


 Cite this: *RSC Adv.*, 2025, 15, 44134

# Green carbon from bagasse for uniform coating of Fe<sub>2</sub>O<sub>3</sub> nanoparticles toward high-capacity and long-life lithium-ion battery anodes

 Quoc Hai Nguyen,<sup>†\*</sup> Chanwoo Park,<sup>†<sup>b</sup></sup> Sang The Chung,<sup>†<sup>c</sup></sup> Thu Huyen Nguyen Thi,<sup>c</sup> To Giang Tran,<sup>de</sup> Jong-Seong Bae,<sup>f</sup> Tuan Loi Nguyen<sup>†<sup>g,h</sup></sup> and Jaehyun Hur<sup>†<sup>g</sup></sup>

Sustainable high-performance anodes are essential for next-generation Li-ion batteries (LIBs). In this study, we develop an Fe<sub>2</sub>O<sub>3</sub>@C composite in which Fe<sub>2</sub>O<sub>3</sub> nanoparticles are uniformly coated with biomass-derived carbon from bagasse—an abundant agricultural residue. Crystalline cellulose extracted from bagasse serves as a green carbon precursor, enabling the formation of a core-shell nanostructure via a simple sol-gel and pyrolysis route. With an optimized Fe<sub>2</sub>O<sub>3</sub>:C weight ratio of 8:2 and a polyacrylic acid binder, the electrode delivers a high reversible capacity of 1893 mA h g<sup>-1</sup> after 100 cycles at 0.1 A g<sup>-1</sup>, retaining 1553 mA h g<sup>-1</sup> after 350 cycles at 0.5 A g<sup>-1</sup>, and exhibits excellent rate capability up to 3 A g<sup>-1</sup>, outperforming many previously reported Fe<sub>2</sub>O<sub>3</sub>-based anodes. This superior performance arises from the synergistic effects of Fe<sub>2</sub>O<sub>3</sub> and the conductive carbon coating, which enhance electron transport, buffer volume expansion, and stabilize the solid electrolyte interphase. This study demonstrates the potential of bagasse valorization for sustainable energy storage and offers a scalable route to high-capacity, long-life LIB anodes, paving the way for eco-friendly and cost-effective electrode production for large-scale applications.

 Received 2nd October 2025  
 Accepted 6th November 2025

DOI: 10.1039/d5ra07487h

[rsc.li/rsc-advances](https://rsc.li/rsc-advances)

## 1 Introduction

The increasing demand for high-performance energy-storage systems has stimulated extensive research on various types of rechargeable batteries, including lithium-ion batteries (LIBs),<sup>1</sup> lithium-metal batteries,<sup>2</sup> lithium/fluorinated carbon batteries,<sup>3</sup> aqueous batteries,<sup>4</sup> zinc-based batteries,<sup>5,6</sup> lithium-oxygen (Li-O<sub>2</sub>) batteries<sup>7,8</sup> and lithium-carbon dioxide (Li-CO<sub>2</sub>) batteries.<sup>9</sup> These technologies are essential for powering modern

electronic devices such as smartphones, laptops, and wearable technologies. Among them, LIBs have gained prominence because of their high energy density, long cycle life, and stable voltage operation.<sup>10,11</sup> However, the limited performance of traditional graphite anodes, with a theoretical capacity of only 372 mA h g<sup>-1</sup>, has driven research on alternative anode materials with higher capacity and superior rate capability.<sup>12</sup> In recent years, transition-metal oxides (TMOs) have emerged as promising candidates for next-generation anode materials in LIBs owing to their high theoretical capacities, diverse oxidation states, and abundance. Compared with conventional graphite anodes, many TMOs, such as Fe<sub>2</sub>O<sub>3</sub>, Co<sub>3</sub>O<sub>4</sub>, and MnO<sub>2</sub>, offer higher capacities exceeding 700 mA h g<sup>-1</sup>. These materials undergo conversion reactions with Li ions, enabling improved energy storage. However, their practical application is limited by issues such as poor electrical conductivity and volume expansion during cycling. To overcome these drawbacks, recent studies have focused on nanostructuring, carbon compositing, and surface modification to enhance the electrochemical performance of TMOs, thereby paving the way for their integration into high-performance LIB systems.<sup>13</sup>

Among TMOs, Fe<sub>2</sub>O<sub>3</sub> has attracted significant attention owing to its high theoretical capacity (~1005 mA h g<sup>-1</sup>), low cost, environmental benignity, and natural abundance.<sup>14,15</sup> Fe<sub>2</sub>O<sub>3</sub> stores Li *via* a conversion reaction, enabling high-energy storage. However, it suffers from major drawbacks such as large

<sup>a</sup>Group of Applied Research in Advanced Materials for Sustainable Development, Faculty of Applied Sciences, Ton Duc Thang University, Ho Chi Minh City, Vietnam. E-mail: [nguyenquochai@tdtu.edu.vn](mailto:nguyenquochai@tdtu.edu.vn)

<sup>b</sup>School of Chemical, Biological, and Battery Engineering, Gachon University, Seongnam, Gyeonggi 13120, Republic of Korea. E-mail: [chanwoo5061@gachon.ac.kr](mailto:chanwoo5061@gachon.ac.kr); [jhhur@gachon.ac.kr](mailto:jhhur@gachon.ac.kr)

<sup>c</sup>Faculty of Applied Sciences, Ton Duc Thang University, Ho Chi Minh City, Vietnam. E-mail: [chungthesang.st@tdtu.edu.vn](mailto:chungthesang.st@tdtu.edu.vn); [nguyenthithuhuyen.st@tdtu.edu.vn](mailto:nguyenthithuhuyen.st@tdtu.edu.vn)

<sup>d</sup>Institute of Research and Development, Duy Tan University, Da Nang, Vietnam. E-mail: [trantogiang@duytan.edu.vn](mailto:trantogiang@duytan.edu.vn)

<sup>e</sup>School of Engineering & Technology, Duy Tan University, Da Nang, Vietnam

<sup>f</sup>Yeongnam Regional Center, Korea Basic Science Institute, Busan 46742, Korea. E-mail: [jsbae@kbsi.re.kr](mailto:jsbae@kbsi.re.kr)

<sup>g</sup>Institute of Fundamental and Applied Sciences, Duy Tan University, Ho Chi Minh City 70000, Vietnam. E-mail: [nguyentuanloi@duytan.edu.vn](mailto:nguyentuanloi@duytan.edu.vn)

<sup>h</sup>Faculty of Natural Sciences, Duy Tan University, Da Nang City 50000, Vietnam

<sup>†</sup> Q. H. Nguyen and C. Park contributed equally to this study.



volume expansion during cycling (>200%), poor intrinsic electrical conductivity, and instability of the solid electrolyte interphase (SEI), which lead to pulverization of the active materials and rapid capacity fading.<sup>16–20</sup> To mitigate these issues, considerable effort has been directed toward the development of Fe<sub>2</sub>O<sub>3</sub>-carbon composites that buffer mechanical stress, enhance electrical conductivity, and stabilize the SEI layer.<sup>21,22</sup>

Among various carbon materials, such as graphene, carbon nanotubes, and soft and hard carbon, biomass-derived carbon is particularly appealing owing to its sustainability, cost-effectiveness, and high structural tunability.<sup>1–3,6,23–26</sup> Bagasse—a major agricultural byproduct in tropical countries such as Vietnam—is particularly attractive as a green carbon precursor. It consists of approximately 40–50 wt% cellulose, 20–30 wt% hemicellulose, and 18–24 wt% lignin, featuring a carbon-rich composition.<sup>25,27</sup> Through pretreatment and pyrolysis, crystalline cellulose (CC) can be extracted from bagasse and converted into conductive, porous, sheet-like carbon with a large surface area and mechanical integrity.<sup>28</sup> These features make bagasse-derived carbon highly suitable for forming core-shell structures with Fe<sub>2</sub>O<sub>3</sub> nanoparticles, as it effectively buffers volume expansion and improves electrochemical kinetics.<sup>16</sup>

In addition to the material composition, electrode binder chemistry plays a crucial role. While polyvinylidene fluoride (PVDF) is the industry standard, its weak van der Waals interactions with active particles and need for toxic solvents such as *N*-methyl-2-pyrrolidone (NMP) reduce mechanical stability and sustainability. In contrast, water-soluble binders such as polyacrylic acid (PAA) can form strong hydrogen bonds with carbon and oxide surfaces, enhancing adhesion, flexibility, and SEI stability.<sup>23,29,30</sup> Few studies have comprehensively investigated the integration of Fe<sub>2</sub>O<sub>3</sub> with sugarcane bagasse (SCB)-derived carbon, particularly in combination with binder engineering. Key challenges remain in optimizing the weight ratio of Fe<sub>2</sub>O<sub>3</sub> to C, controlling particle size, ensuring uniform carbon coating, and improving long-term cycling stability at practical current densities.

In this work, we report the synthesis of Fe<sub>2</sub>O<sub>3</sub>@C nanocomposites using Fe(NO<sub>3</sub>)<sub>3</sub> and CC derived from SCB *via* two facile steps, including sol-gel and pyrolysis methods. Three composite ratios (8 : 2, 7 : 3, and 5 : 5) were tested. The effects of the carbon content and binder type (PVDF and PAA) on the structural and electrochemical properties of the resulting materials were systematically studied. Our results demonstrate that SCB-derived carbon facilitates the formation of a robust core-shell architecture, resulting in enhanced Li storage capacity, excellent rate capability, and long-term cycling stability. Thus, it is a promising candidate for next-generation LIB anodes.

Although Fe<sub>2</sub>O<sub>3</sub>@C composites have been widely investigated as anode materials, most previous studies relied on synthetic carbon sources such as graphene, CNTs, or polymer-derived carbon, *etc.*, and often involving complicated synthesis and high costs. In contrast, this work introduces a sustainable and facile strategy by using sugarcane bagasse, a low-cost agricultural byproduct, as the carbon precursor through a simple sol-gel and pyrolysis route. Moreover, we

systematically optimized the Fe<sub>2</sub>O<sub>3</sub>:C ratio and employed a water-soluble PAA binder instead of PVDF, resulting in improved electrode adhesion and structural stability. These strategies yield remarkable electrochemical performance (1893 mA h g<sup>-1</sup> after 100 cycles at 0.1 A g<sup>-1</sup> and 1553 mA h g<sup>-1</sup> after 350 cycles at 0.5 A g<sup>-1</sup>), surpassing most reported Fe<sub>2</sub>O<sub>3</sub>@C works. The superior behavior originates from the synergistic effects of the uniform biomass-derived carbon coating and the flexible PAA binder, which together enhance conductivity, buffer volume expansion, and stabilize the SEI layer. Therefore, this study provides both a sustainable materials concept and an improved electrochemical mechanism for achieving long-life and high-capacity Fe<sub>2</sub>O<sub>3</sub>-based lithium-ion battery anodes.

## 2 Experimental section

### 2.1 Materials

Bagasse from Vietnam was collected, washed, dried, and ground into powder. Iron(III) nitrate nonahydrate (Fe(NO<sub>3</sub>)<sub>3</sub>·9H<sub>2</sub>O, 98%, Sigma-Aldrich), ethylene glycol (EG, 99%, JHD GHTECH), oxalic acid dihydrate (H<sub>2</sub>C<sub>2</sub>O<sub>4</sub>·2H<sub>2</sub>O, 99.5%, JHD GHTECH), acetic acid (C<sub>2</sub>H<sub>4</sub>O<sub>2</sub>, 99.5%, JHD GHTECH), hydrogen peroxide (H<sub>2</sub>O<sub>2</sub>, 30%, Xilong), sulfuric acid (H<sub>2</sub>SO<sub>4</sub>, 98%, Vietnam), and sodium hydroxide (NaOH, 98%, Vietnam) were of analytical grade and used without further purification.

### 2.2 Extraction of crystalline cellulose (CC) from bagasse

The powdered bagasse was first bleached *via* sequential treatment with acetic acid (80 wt%, 80 °C, 2 h) and hydrogen peroxide (20 wt%, 80 °C, 2 h) to eliminate lignin and hemicellulose. The resulting cellulose pulp was subsequently washed with deionized (DI) water and hydrolyzed with sulfuric acid (60 wt%) under reflux at 60 °C for 2 h to remove amorphous regions. The final product was filtered, washed repeatedly to achieve a neutral pH, and freeze-dried at -40 °C for 8 h to obtain CC powder.

### 2.3 Synthesis of Fe<sub>2</sub>O<sub>3</sub>@C composites

First, Fe(NO<sub>3</sub>)<sub>3</sub>·9H<sub>2</sub>O (1 M) was dissolved in a mixture of oxalic acid (1 M) and ethylene glycol (1 M) at a volumetric ratio of 1 : 1 to prepare the Fe precursor solution. Subsequently, the extracted CC was added and dispersed under stirring to obtain a uniform suspension. Three samples of Fe<sub>2</sub>O<sub>3</sub>@C composites with different weight ratios of Fe<sub>2</sub>O<sub>3</sub> to carbon (8 : 2, 7 : 3, and 5 : 5) were prepared by mixing the calculated amounts of Fe precursor and cellulose suspension. The resulting mixture was ultrasonicated at 300 W for 30 min to ensure homogeneous dispersion, followed by aging at 90 °C under continuous stirring (600 rpm) until gelation occurred. The gel was dried at 100 °C overnight to remove residual solvent, followed by pyrolysis in a tubular furnace under an N<sub>2</sub> atmosphere at 450 °C for 6 h. This thermal treatment resulted in the formation of an Fe<sub>2</sub>O<sub>3</sub>@C composite with a core-shell structure, where Fe<sub>2</sub>O<sub>3</sub> nanoparticles were uniformly coated by carbon derived from bagasse. For comparison, pure-Fe<sub>2</sub>O<sub>3</sub> powder was prepared using the same procedure without adding CC solution, and the



bagasse-derived carbon was obtained *via* thermal treatment of CC powder at 450 °C for 6 h.

#### 2.4 Electrode preparation and electrochemical characterization

The working electrode was prepared by mixing Fe<sub>2</sub>O<sub>3</sub>@C, Super P carbon black, and binder (either PVDF or PAA) in a weight ratio of 8 : 1 : 1. NMP was used as the solvent for the PVDF-based electrodes, and DI water was used for the PAA-based electrodes. The slurry was cast onto Cu foil using a doctor blade and dried at 80 °C under vacuum for 12 h. CR2032-type coin cells were assembled in an Ar-filled glove box using Li foil as the counter electrode, a polypropylene membrane as the separator, and 1 M LiPF<sub>6</sub> in ethylene carbonate: diethylene carbonate (1 : 1 v/v) as the electrolyte. The typical active material and electrolyte loading was 1.0–1.2 mg cm<sup>-2</sup> and 120 μL for each cell. Galvanostatic charge/discharge (GCD) tests were conducted using a battery tester in the voltage range of 0.01–3.0 V (*vs.* Li<sup>+</sup>/Li). Cyclic voltammetry (CV) and electrochemical impedance spectroscopy (EIS) were performed to evaluate the redox behavior and charge-transfer resistance.

#### 2.5 Material characterization

The structural, morphological, and surface properties of the synthesized Fe<sub>2</sub>O<sub>3</sub>@C composites were characterized using various techniques. X-ray diffraction (XRD) analysis was performed using a Bruker D8 Advance diffractometer with Cu Kα radiation ( $\lambda = 1.5406 \text{ \AA}$ ), operated at 40 kV and 40 mA over the  $2\theta$  range of 10–80°. Scanning electron microscopy (SEM) (Hitachi S-4800) and high-resolution transmission electron microscopy (HRTEM) (JEOL JEM-2100) were employed to

examine the surface morphology, particle size, and distribution of Fe<sub>2</sub>O<sub>3</sub> within the carbon matrix. Energy-dispersive X-ray spectroscopy (EDS) coupled with SEM was used for elemental mapping to confirm the spatial distribution of Fe, O, and C in the composites. N<sub>2</sub> adsorption–desorption measurements were performed at 77 K using a Micromeritics ASAP 2020 instrument. The Brunauer–Emmett–Teller (BET) method was used to calculate the specific surface area, and the Barrett–Joyner–Halenda (BJH) model was used to determine the pore size distribution from the desorption branch of the isotherm. The chemical state study of etch elements were performed high-performance X-ray photoelectron spectroscopy: HP-XPS (BS101), K-ALPHA+, Thermo Fisher Scientific Inc. (UK) using monochromated Al Kα X-ray source ( $h\nu = 1486.6 \text{ eV}$ , power = 12 kV, 72 W) at a spot size of 400 μm in diameter with charge compensation using two flood gun (low energy electron and Ar<sup>+</sup> ion) at Yeongnam Regional Center of Korea Basic Science Institute (KBSI).

### 3 Results and discussion

The synthesis process of the Fe<sub>2</sub>O<sub>3</sub>@C nanoparticles is illustrated in Fig. 1 and described in the Experimental Section. The formation of the Fe<sub>2</sub>O<sub>3</sub>@C composite is governed by a sol–gel process during the mixing and aging steps. Initially, Fe<sup>3+</sup> ions from Fe(NO<sub>3</sub>)<sub>3</sub>·9H<sub>2</sub>O interact with oxalic acid to form Fe–oxalate complexes, preventing premature precipitation of Fe(OH)<sub>3</sub>. EG functions as a polyol, promoting esterification and polycondensation reactions with oxalic acid. Heating at 90 °C forms an organic polymeric network that traps Fe<sup>3+</sup> species uniformly within the gel matrix. This gelation step ensures the

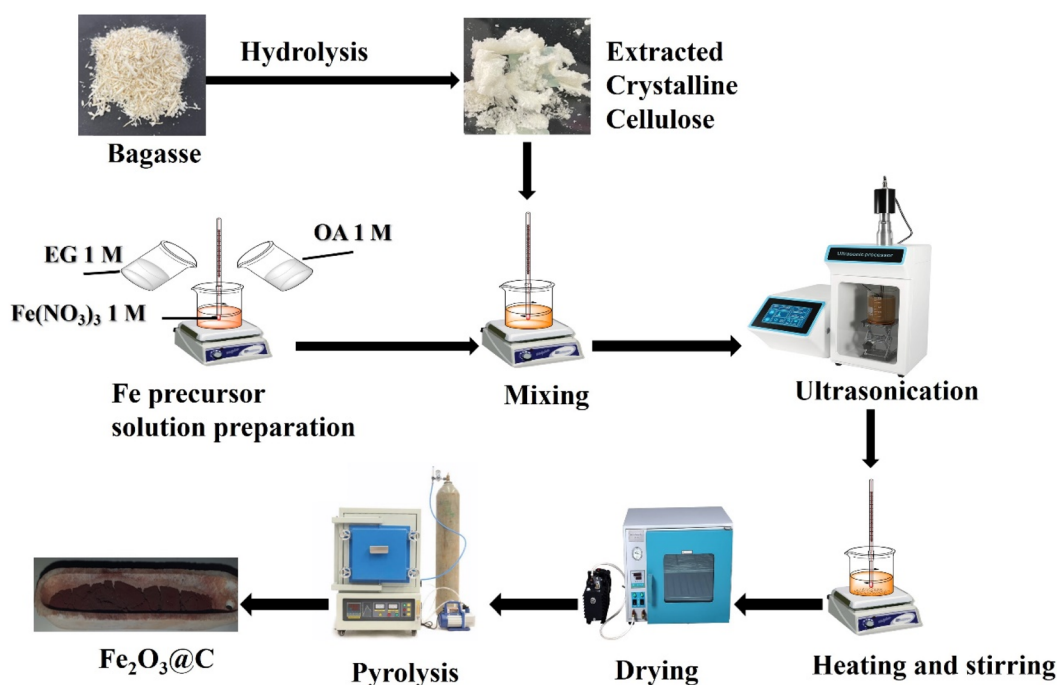


Fig. 1 Scheme of synthesis of core–shell Fe<sub>2</sub>O<sub>3</sub>@C nanoparticles.



homogeneous distribution of the Fe precursor and cellulose within the network. Upon drying and pyrolysis under  $N_2$ , the carbon-phase component derived from CC is formed *via* pyrolysis (eqn (1)),<sup>28,31</sup> while the coordinated  $Fe^{3+}$  species is converted to  $Fe_2O_3$  nanoparticles *via* two steps, as given by eqn (2) and (3), resulting in a core-shell structure where carbon derived from cellulose encapsulates  $Fe_2O_3$  nanoparticles.<sup>32</sup>

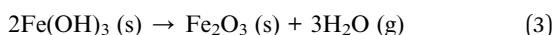
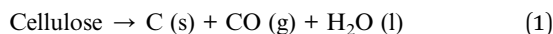


Fig. 2 shows the XRD patterns of the bagasse-derived carbon, pure  $Fe_2O_3$ , and the  $Fe_2O_3@C$  composites (8 : 2, 7 : 3, and 5 : 5). The  $Fe_2O_3$ -based samples exhibited sharp diffraction peaks at  $2\theta \approx 24.1^\circ$ ,  $33.2^\circ$ ,  $35.6^\circ$ ,  $40.9^\circ$ ,  $49.5^\circ$ ,  $54.1^\circ$ ,  $57.7^\circ$ ,  $62.4^\circ$ , and  $64.0^\circ$ , corresponding to the (012), (104), (110), (113), (024), (116), (018), (214), and (300) crystal planes of rhombohedral hematite  $Fe_2O_3$  (JCPDS no. 33-0664), respectively. These results confirmed the formation of the high-crystallinity phase  $\alpha\text{-Fe}_2\text{O}_3$ . In contrast, the bagasse-derived carbon exhibited a broadened peak at  $2\theta \approx 22^\circ$ , characteristic of amorphous carbon derived from biomass pyrolysis.<sup>33,34</sup> For comparison, the (002) reflection of graphitic carbon (PDF#41-1487) is typically observed at  $2\theta \approx 26.2^\circ$ . The absence of this distinct peak in our samples confirms that the bagasse-derived carbon remains largely amorphous. In addition, all  $Fe_2O_3@C$  samples exhibited only a faint hump at  $2\theta \approx 20\text{--}25^\circ$ , corresponding to cellulose-derived carbon, which remained predominantly amorphous after pyrolysis at  $450^\circ\text{C}$  under  $N_2$ . This weak feature was obscured by the sharp diffraction peaks of  $Fe_2O_3$ . With increasing  $Fe_2O_3$  crystallinity, the strong diffraction of  $Fe_2O_3$  dominated the diffractogram, effectively masking the carbon signal. Moreover, a new weak peak at  $\sim 31^\circ$  appeared, which can be assigned to the (220) plane of a spinel iron oxide ( $\gamma\text{-Fe}_2\text{O}_3$  or  $Fe_3O_4$ ), formed *via* partial

thermal reduction of  $Fe(III)$  species in the carbonaceous matrix during thermal treatment under  $N_2$  at  $450^\circ\text{C}$ .<sup>35</sup> Among the composite samples,  $Fe_2O_3@C(8 : 2)$  exhibited the most intense and well-defined diffraction peaks of carbon, suggesting that the moderate carbon content allowed optimal crystallite growth.  $Fe_2O_3@C(7 : 3)$  exhibited slightly reduced peak intensities, and  $Fe_2O_3@C(5 : 5)$  exhibited broader peaks with reduced intensities, indicating a tendency to transform into amorphous carbon with an increase in carbon content. No secondary phases or impurities (such as  $Fe_3O_4$  or Fe) were detected, confirming the high purity of the  $Fe_2O_3$  materials. This structural integrity is essential for achieving stable conversion reactions during lithiation/delithiation in LIBs.

The surface morphologies of the as-prepared samples were examined using SEM, as shown in Fig. 3. These images reveal the structural differences among the bagasse-derived carbon, pure  $Fe_2O_3$ , and  $Fe_2O_3@C$  nanocomposites synthesized at various  $Fe_2O_3 : C$  mass ratios. Fig. 3a shows that the carbon obtained from bagasse pyrolysis has a thin, wrinkled, and layered sheet-like morphology in micro size, which is typical for biomass-derived carbon materials. This porous structure increases the surface area and provides a network for dispersing and covering smaller particles.<sup>36</sup> In contrast, the pure- $Fe_2O_3$  sample (Fig. 3b) exhibited dense and aggregated spherical nanoparticles with poor dispersion. This agglomeration is attributed to strong magnetic-dipole interactions and surface energy, which can lead to poor electrochemical performance owing to hindered  $Li^+$  diffusion and limited active sites.<sup>37</sup>

The introduction of carbon significantly altered the morphologies of the composites.  $Fe_2O_3@C(5 : 5)$  (Fig. 3c) exhibited irregularly dispersed particles within a relatively thick carbon matrix. Excess carbon likely led to partial encapsulation of the active material, reducing the accessibility of  $Fe_2O_3$  to the electrolyte and potentially hindering electron transfer.  $Fe_2O_3@C(7 : 3)$  (Fig. 3d) exhibited moderate dispersion of  $Fe_2O_3$  nanoparticles with reduced agglomeration. The particles appeared to be more evenly distributed within the carbon framework, indicating improved structural integration.  $Fe_2O_3@C(8 : 2)$  (Fig. 3e) exhibited the most homogeneous and uniform distribution of  $Fe_2O_3$  nanoparticles, which were well-dispersed within a thin carbon matrix, forming a favorable core-shell configuration, as confirmed by the transmission electron microscopy (TEM) images in Fig. 4c and d. This optimized morphology is expected to facilitate ion and electron transport and buffer mechanical stress during cycling, leading to enhanced electrochemical performance.<sup>16,29</sup> In addition, the particle size distributions of the  $Fe_2O_3@C$  samples were examined (Fig. 3f and S1), revealing the smallest average particle diameter ( $\sim 75.38 \pm 12.65$  nm) for the  $Fe_2O_3@C(8 : 2)$  sample, compared to  $\sim 84.43 \pm 7.73$  nm for  $Fe_2O_3@C(7 : 3)$  and  $\sim 100.04 \pm 14.28$  nm for  $Fe_2O_3@C(5 : 5)$ . The relatively narrow size distribution of all samples indicates effective control over nucleation and growth during synthesis, which is crucial for achieving stable cycling performance and high rate capability.<sup>14</sup> Notably, the smallest particle size of  $Fe_2O_3@C(8 : 2)$  suggests that its thinner carbon layer—resulting from the lower carbon

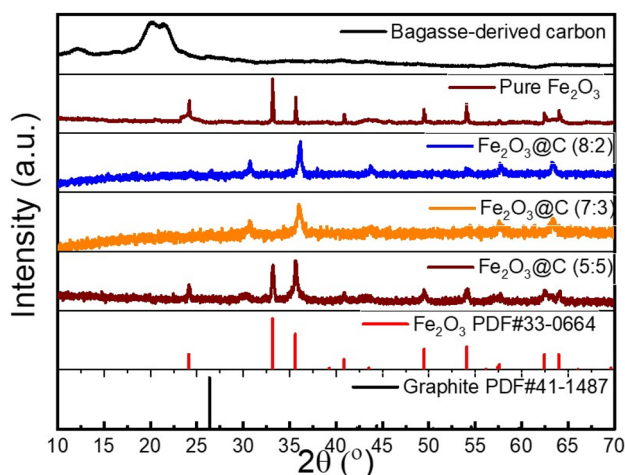


Fig. 2 XRD patterns of  $Fe_2O_3@C$  with various ratios (5 : 5, 7 : 3, and 8 : 2), pure  $Fe_2O_3$ , and bagasse-derived carbon.



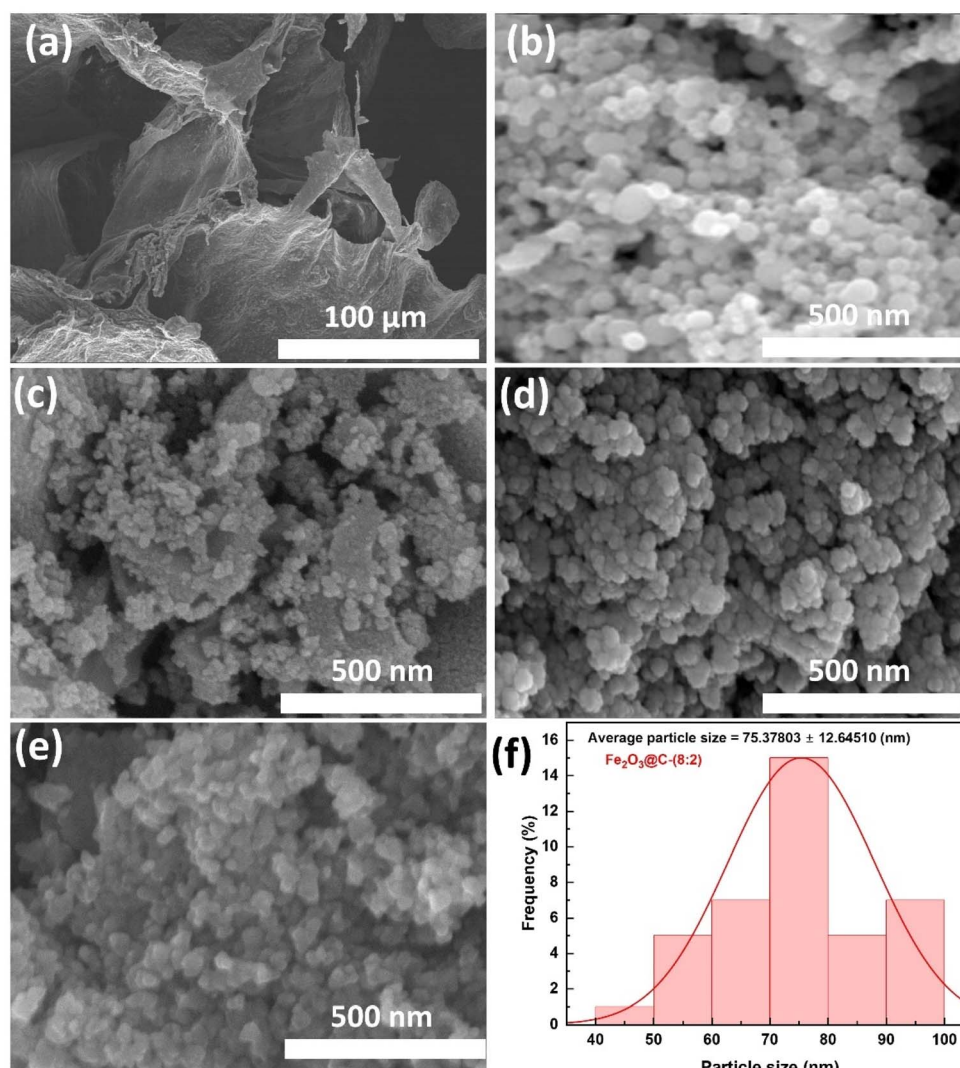


Fig. 3 SEM images of (a) bagasse-derived carbon, (b) pure  $\text{Fe}_2\text{O}_3$ , (c)  $\text{Fe}_2\text{O}_3@\text{C}$ -(5 : 5), (d)  $\text{Fe}_2\text{O}_3@\text{C}$ -(7 : 3), and (e)  $\text{Fe}_2\text{O}_3@\text{C}$ -(8 : 2); (f) particle size distribution of  $\text{Fe}_2\text{O}_3@\text{C}$ -(8 : 2).

content—may facilitate faster charge transfer by reducing the interfacial resistance during charge/discharge processes.

To further investigate the nanostructure and composition of the synthesized  $\text{Fe}_2\text{O}_3@\text{C}$  composites, BET surface area analysis, EDS mapping, and HRTEM were employed. The  $\text{N}_2$  adsorption-desorption isotherms (Fig. 4a) indicated that  $\text{Fe}_2\text{O}_3@\text{C}$ -(8 : 2) had a significantly larger specific surface area ( $157.1 \text{ m}^2 \text{ g}^{-1}$ ) than  $\text{Fe}_2\text{O}_3@\text{C}$ -(5 : 5) ( $30.3 \text{ m}^2 \text{ g}^{-1}$ ) and  $\text{Fe}_2\text{O}_3@\text{C}$ -(7 : 3) ( $51.3 \text{ m}^2 \text{ g}^{-1}$ ). This is attributed to the optimized carbon content, which prevents  $\text{Fe}_2\text{O}_3$  nanoparticle agglomeration and forms a porous carbon matrix. A larger surface area provides more active sites for Li storage and enhances the electrolyte infiltration, leading to improved electrochemical kinetics.<sup>21</sup> In addition, Fig. 4b shows the EDS elemental mapping of  $\text{Fe}_2\text{O}_3@\text{C}$ -(8 : 2), which confirms the uniform distribution of Fe, O, and C throughout the composite. The even dispersion of Fe and O indicates homogeneous formation of  $\text{Fe}_2\text{O}_3$  nanograins, while the surrounding carbon matrix ensures continuous

electrical contact. This compositional uniformity plays a key role in maintaining structural stability during repeated charge/discharge cycles.<sup>38</sup> Moreover, the TEM image in Fig. 4c reveals discrete  $\text{Fe}_2\text{O}_3$  nanoparticles embedded within a thin carbon matrix, consistent with a well-dispersed core-shell architecture. The particles were quasi-spherical and exhibited minimal aggregation, which was consistent with the SEM and BET observations. Furthermore, an HRTEM image (Fig. 4d) showed that this material consisted of  $\text{Fe}_2\text{O}_3$  particles encapsulated in carbon. The spacing between the lattice planes was determined to be approximately 0.258 nm, corresponding to the (110) plane of the  $\text{Fe}_2\text{O}_3$  material. The core-shell structure comprised a crystalline  $\text{Fe}_2\text{O}_3$  core surrounded by a carbon shell with a thickness of approximately 10 nm. The carbon layer is continuous and wraps the  $\text{Fe}_2\text{O}_3$  core, which helps accommodate volume expansion, maintain electrical connectivity, and suppress the pulverization effect common in TMO anodes.<sup>18</sup>



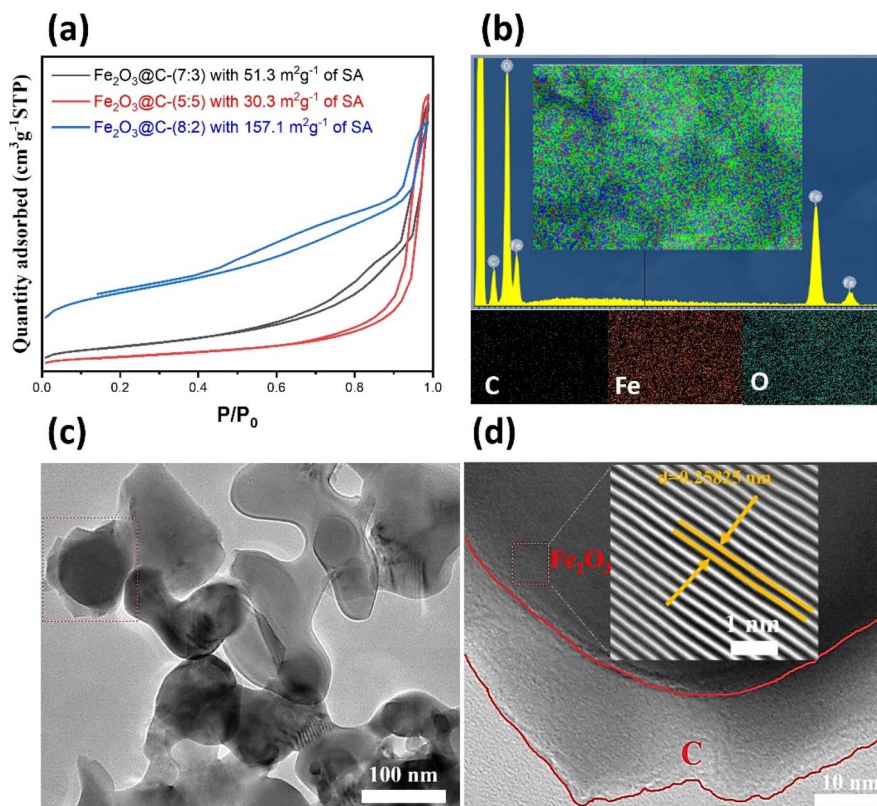


Fig. 4 (a)  $N_2$  adsorption–desorption isotherms (BET surface area) of  $Fe_2O_3@C$  composites; (b) EDS elemental mapping of  $Fe_2O_3@C-(8:2)$ ; (c and d) TEM and HRTEM images of  $Fe_2O_3@C-(8:2)$ , showing a core–shell  $Fe_2O_3$ –C architecture.

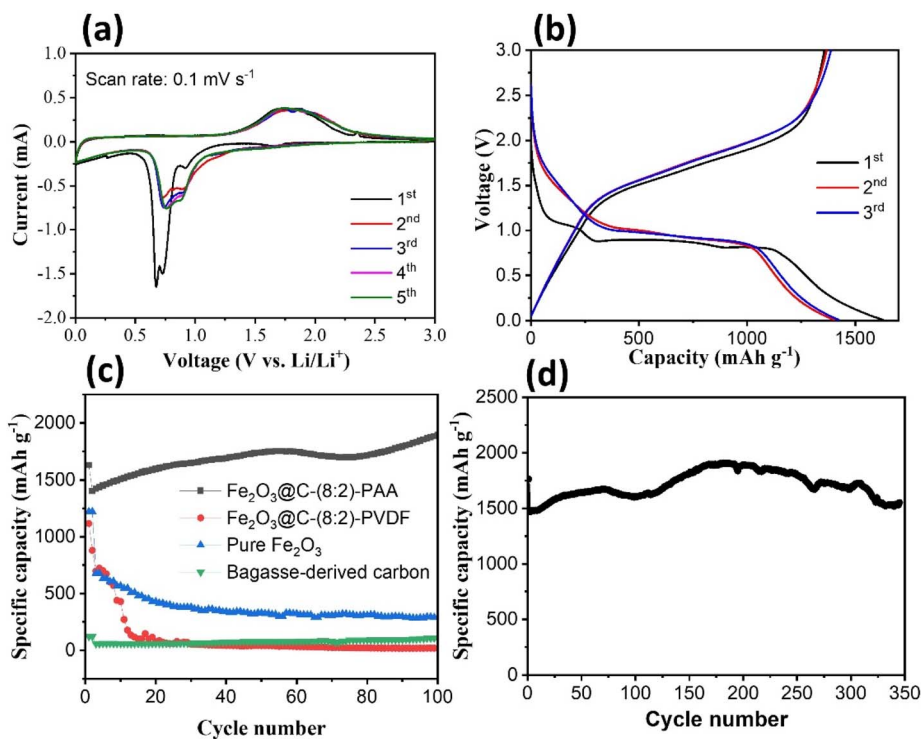


Fig. 5 (a) CV curves at  $0.1 \text{ mV s}^{-1}$ ; (b) charge/discharge profiles of the  $Fe_2O_3@C-8:2$  composite at  $0.1 \text{ A g}^{-1}$  during the first three cycles; (c) cycling performance at  $0.1 \text{ A g}^{-1}$  of different  $Fe_2O_3@C$  composites; (d) long-term cycling performance of  $Fe_2O_3@C-8:2$  at  $0.5 \text{ A g}^{-1}$ .



The CV and GCD tests (Fig. 5a and b) were performed to evaluate the electrochemical behavior of the Fe<sub>2</sub>O<sub>3</sub>@C composites. The CV curves of Fe<sub>2</sub>O<sub>3</sub>@C were recorded at a scan rate of 0.1 mV s<sup>-1</sup> in the voltage window of 0.01–3.0 V vs. Li/Li<sup>+</sup> (Fig. 5a). In the first cathode scan, the peaks at ~0.92, ~0.72, and ~0.67 V are attributed to the insertion of ions Li<sup>+</sup> into the structure of the Fe<sub>2</sub>O<sub>3</sub> material (eqn (4)), the reduction of Fe(III) to Fe(0) (eqn (5)), and the development of the SEI layer, respectively. The disappearance of the peak at ~0.67 V in subsequent cycles indicated that the SEI formation was irreversible. The cathode peaks in the subsequent cycles exhibited a shift in position compared to the first cycle, specifically at ~0.9 and ~0.75 V. This phenomenon may be related to the formation of an SEI layer during the first cycle. In contrast, the anode peak exhibited consistent oxidation-peak positions in all five cycles. The broad peak appearing at ~1.75 V may represent the transition from Fe<sup>0</sup> to Fe<sup>3+</sup>.<sup>39–41</sup> In addition, the overlap of the CV curves was almost identical after the first discharge cycle, which suggests the good reversible redox behavior of the Fe<sub>2</sub>O<sub>3</sub>@C electrode. The electrochemical reaction mechanism of the Fe<sub>2</sub>O<sub>3</sub>@C composite can be summarized as follows:

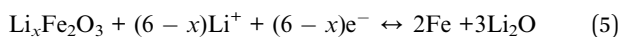


Fig. 5b presents the voltage profile of the Fe<sub>2</sub>O<sub>3</sub>@C electrode during the first three cycles at a current density of 0.1 A g<sup>-1</sup>, which exhibits characteristic plateaus, consistent with the CV results. The first discharge capacity exceeds 1627 mA h g<sup>-1</sup> but with irreversible capacity loss due to SEI formation and electrolyte decomposition, corresponding to a coulombic efficiency of ~83%.<sup>42</sup> The reversible capacity stabilizes at ~1406 mA h g<sup>-1</sup> from the second cycle onward, and the coulombic efficiency increases to ~98% for the second and third cycles. The relatively flat discharge plateau near ~0.9, ~0.8, and ~0.6 V and the charge plateau near ~1.75 V confirm the conversion-type reaction mechanism revealed by CV analysis. Voltage hysteresis between charge and discharge is typical for Fe<sub>2</sub>O<sub>3</sub> anodes and can be mitigated by the carbon matrix, which enhances conductivity and structural integrity. The aforementioned findings indicated the good reversible discharge capability of the Fe<sub>2</sub>O<sub>3</sub>@C electrode.

The cycling performance of the Fe<sub>2</sub>O<sub>3</sub>@C electrode at a current density of 0.1 A g<sup>-1</sup> was evaluated in comparison with pure Fe<sub>2</sub>O<sub>3</sub> and bagasse-derived carbon, along with the effect of the binder on the Fe<sub>2</sub>O<sub>3</sub>@C electrode (Fig. 5c). The electrodes prepared with the PVDF binder for Fe<sub>2</sub>O<sub>3</sub>@C, pure Fe<sub>2</sub>O<sub>3</sub>, and bagasse-derived carbon exhibited a sharp decline in capacity after just a few cycles. Among them, the carbon electrode exhibited a low capacity of ~121 mA h g<sup>-1</sup> at the 1st cycle, and its capacity remained at ~108 mA h g<sup>-1</sup> after the 100th cycle. The pure-Fe<sub>2</sub>O<sub>3</sub> electrode exhibited the highest specific capacity at the first cycle (~1221 mA h g<sup>-1</sup>), compared to ~1116 mA h g<sup>-1</sup> for Fe<sub>2</sub>O<sub>3</sub>@C; however, this value was reduced to 632 mA h g<sup>-1</sup> after five cycles, which was lower than the capacity of Fe<sub>2</sub>O<sub>3</sub>@C

(701 mA h g<sup>-1</sup>). The significant capacity loss for the pure-Fe<sub>2</sub>O<sub>3</sub> electrode could be due to the large volume expansion of the electrode material after repeated charge/discharge cycles, which destroyed the structure of the material. Moreover, the specific capacity of Fe<sub>2</sub>O<sub>3</sub>@C using the PVDF binder continued to decrease significantly over 100 cycles, reaching ~17.5<sup>-1</sup> mA h g<sup>-1</sup>, primarily because of the mechanical and interfacial limitations of the PVDF binder when paired with conversion-type anode materials such as Fe<sub>2</sub>O<sub>3</sub>. First, PVDF lacks sufficient elasticity to accommodate large volume variations of Fe<sub>2</sub>O<sub>3</sub> during lithiation/delithiation (>200%) in conversion-type anodes, leading to cracking and pulverization of the electrode and loss of electrical contact between active-material particles and the current collector.<sup>43</sup> Second, PVDF is nonpolar and chemically inert, offering weak interfacial binding with metal-oxide surfaces such as Fe<sub>2</sub>O<sub>3</sub>. This contributes to poor adhesion and structural instability during repeated cycling, resulting in Fe<sub>2</sub>O<sub>3</sub> particles being detached from the electrode matrix and becoming electrochemically inactive owing to poor electronic connectivity. In contrast, the Fe<sub>2</sub>O<sub>3</sub>@C electrode using the PAA binder exhibited a specific capacity of 1627 mA h g<sup>-1</sup> at the first cycle, and this value tended to increase during the discharge process, reaching 1893 mA h g<sup>-1</sup> at the 100th cycle. PAA forms strong hydrogen bonds with oxide surfaces, which improves the mechanical integrity and adhesion of the electrodes compared to PVDF.<sup>44</sup> Moreover, PAA exhibits elastic and ductile mechanical behavior, allowing it to maintain electrode integrity under significant morphological changes, whereas PVDF is relatively brittle and less resilient.<sup>45,46</sup> Furthermore, PAA interacts more effectively with conductive additives, such as carbon, facilitating the formation of a continuous conductive network. This enhancement promotes charge transfer and electronic conductivity throughout the electrode, which is crucial for Fe<sub>2</sub>O<sub>3</sub> because of its intrinsically low conductivity. When the charge/discharge process was performed at a high current density of 0.5 A g<sup>-1</sup> (Fig. 5d), the Fe<sub>2</sub>O<sub>3</sub>@C-(8:2) electrode still exhibited a remarkable capacity of ~1552 mA h g<sup>-1</sup> after 350 cycles. This stability stems from the core-shell structure and optimal carbon content (20 wt%), which effectively buffer the large volume changes of Fe<sub>2</sub>O<sub>3</sub> and preserve the structural integrity of the electrode.<sup>47,48</sup>

Fig. 6a demonstrates the impact of the Fe<sub>2</sub>O<sub>3</sub>:C mass ratio on the cycling stability of the composite electrodes. The Fe<sub>2</sub>O<sub>3</sub>@C-(8:2) electrode exhibited a specific capacity of 1627 mA h g<sup>-1</sup> at the first cycle, and this value tended to increase during the discharge process, reaching 1893 mA h g<sup>-1</sup> at the 100th cycle. Similarly, the specific capacity of the Fe<sub>2</sub>O<sub>3</sub>@C-(7:3) and Fe<sub>2</sub>O<sub>3</sub>@C-(5:5) electrodes increased to ~1624 and ~1070 mA h g<sup>-1</sup>, respectively, after 100 discharge cycles. This enhancement is primarily attributed to the structural integrity and strong interfacial contact between Fe<sub>2</sub>O<sub>3</sub> and the biomass-derived carbon matrix. In contrast to conventional carbon additives, carbon from bagasse forms a continuous and flexible network that accommodates volume changes, suppresses particle pulverization, and maintains electronic conductivity. The superior performance of Fe<sub>2</sub>O<sub>3</sub>@C-(8:2) compared to Fe<sub>2</sub>O<sub>3</sub>@C-(7:3) and Fe<sub>2</sub>O<sub>3</sub>@C-(5:5) is ascribed to



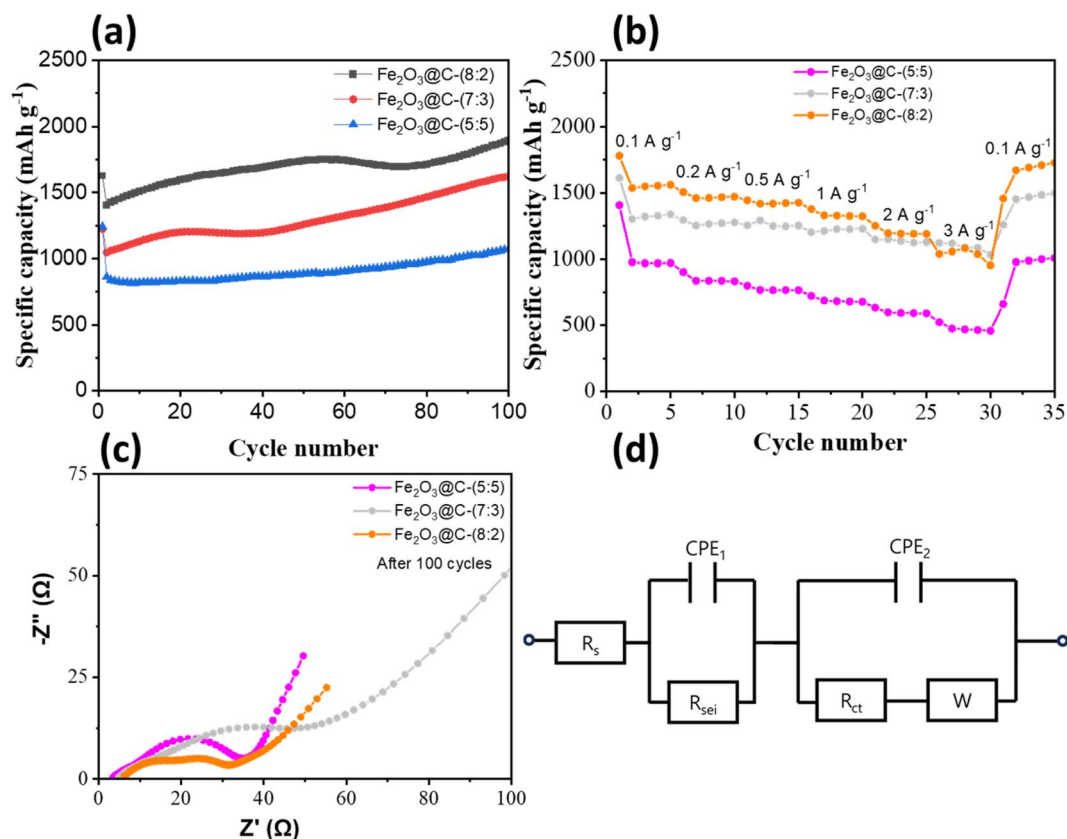


Fig. 6 (a) Cycling performance at a current density of  $0.1 \text{ A g}^{-1}$  of  $\text{Fe}_2\text{O}_3@\text{C}$  composites with different  $\text{Fe}_2\text{O}_3$ -to-carbon mass ratios; (b) rate capability of  $\text{Fe}_2\text{O}_3@\text{C}$  composites; (c) EIS plots of  $\text{Fe}_2\text{O}_3@\text{C}$  electrodes after the cycling test; (d) equivalent circuit model.

the optimal carbon content, which provides sufficient electronic pathways and structural cushioning without excessively diluting the active-material ( $\text{Fe}_2\text{O}_3$ ) content. Excess carbon reduces the volumetric energy density and prevents aggregation and cracking during cycling.<sup>16</sup> The gradual capacity increase during cycling observed in Fig. 5c and 6a can be ascribed to the electrode activation process, including gradual wetting and penetration of the electrolyte; the reversible formation of polymeric gel-like films, which contribute pseudocapacitive capacity; enhanced reversibility of the conversion reaction due to structural rearrangements of  $\text{Fe}_2\text{O}_3@\text{C}$  nanocomposite and increased electronic conductivity from the carbon coating. This behavior is intrinsic to  $\text{Fe}_2\text{O}_3$ -based anodes and is not caused by electrolyte consumption, as confirmed by the reduced  $R_{\text{ct}}$  observed in the EIS.<sup>13,16,17,37,49</sup>

Furthermore, as shown in Fig. 6b, the rate capability of the composite electrodes is evaluated at increasing current densities ranging from  $0.1$  to  $3 \text{ A g}^{-1}$ . Owing to diffusion limitations, the capacity of the  $\text{Fe}_2\text{O}_3@\text{C}(8:2)$  electrode decreased gradually from  $1780 \text{ mA h g}^{-1}$  to  $1506$ ,  $1444$ ,  $1376$ ,  $1251$ , and  $1038 \text{ mA h g}^{-1}$  as the current increased from  $0.1 \text{ A g}^{-1}$  to  $0.2$ ,  $0.5$ ,  $1$ ,  $2$ , and  $3 \text{ A g}^{-1}$ , respectively, but it quickly recovered to  $\sim 1726 \text{ mA h g}^{-1}$  when the current was returned to  $0.1 \text{ A g}^{-1}$ . Although the specific capacities were lower owing to the lower mass of  $\text{Fe}_2\text{O}_3$  in the composite, the rate capability of the samples with ratios of  $7:3$  and  $5:5$  exhibited the same

properties (good recovery of capacitance after a series of current density) as that of the  $(8:2)$  sample. This excellent rate performance of all samples is attributed to (1)  $\text{Fe}_2\text{O}_3$  nanoparticles that shorten  $\text{Li}^+$  diffusion paths; (2) the uniform carbon coating derived from bagasse, which enhances electrical conductivity; and (3) the porous morphology, as confirmed by BET and TEM analysis, which allows electrolyte penetration and efficient ion transport. These results confirm that the core-shell structure of  $\text{Fe}_2\text{O}_3@\text{C}$  with the bagasse-derived carbon shell not only enhances long-term durability but also provides outstanding rate performance, which is critical for practical LIB applications where both power and stability are essential. This result is superior to those for most other  $\text{Fe}_2\text{O}_3$ -carbon composite anodes in previous works, as summarized in Table S1.

EIS was conducted after 100 cycles to gain insights into the interfacial resistance and charge-transfer kinetics of  $\text{Fe}_2\text{O}_3@\text{C}$  electrodes with different  $\text{Fe}_2\text{O}_3$ :carbon ratios (Fig. 6c). The fitted parameters based on the equivalent circuit (Fig. 6d) are presented in Table S1, including the solution resistance ( $R_s$ ), SEI resistance ( $R_{\text{SEI}}$ ), and charge-transfer resistance ( $R_{\text{ct}}$ ).  $R_s$  increased significantly as the carbon content decreased, rising from  $3.2 \Omega$  ( $\text{Fe}_2\text{O}_3@\text{C}(5:5)$ ) to  $5.8 \Omega$  ( $\text{Fe}_2\text{O}_3@\text{C}(7:3)$ ) and  $6.6 \Omega$  ( $\text{Fe}_2\text{O}_3@\text{C}(8:2)$ ). This minor variation compared with  $R_{\text{ct}}$  suggests that the electrolyte resistance had a negligible influence on performance. In addition, the increase in  $R_s$  compared to fresh cells (Table S2) likely originated from the reduced



porosity and additional SEI formation on the Fe<sub>2</sub>O<sub>3</sub>-rich electrodes after cycling.<sup>12,17</sup> Notably,  $R_{ct}$  exhibited the opposite trend to that for the fresh cells (Fig. S2). It decreased with a lower carbon content after cycling. The Fe<sub>2</sub>O<sub>3</sub>@C-(8:2) electrode exhibited the lowest  $R_{ct}$  (8.5 Ω) after 100 cycles, whereas the carbon-rich sample (Fe<sub>2</sub>O<sub>3</sub>@C-(5:5)) exhibited the highest  $R_{ct}$  (180.5 Ω). This indicates that Fe<sub>2</sub>O<sub>3</sub>-rich electrodes undergo structural reorganization during cycling, generating finely dispersed metallic Fe and a stable SEI, which enhance electronic conductivity and interfacial kinetics. In contrast, excessive carbon promotes partial electrode densification and unstable SEI growth, increasing the interfacial resistance during cycling.<sup>49,50</sup> For all the samples,  $R_{SEI}$  was increased after cycling, reflecting ongoing SEI formation and electrolyte decomposition. This increase was most significant for the Fe<sub>2</sub>O<sub>3</sub>@C-(5:5) electrode because of its large carbon surface area, which accelerated SEI thickening. In comparison, the Fe<sub>2</sub>O<sub>3</sub>@C-(8:2) electrode developed a thinner and more stable SEI, contributing to improved cycling stability and rate performance. In addition, Fig. S3 shows the morphologies of the Fe<sub>2</sub>O<sub>3</sub>@C-(8:2) electrodes before and after cycling. Although SEI was formed after cycling test, the presence of a thin and uniform SEI layer could be evidenced by the low charge-transfer resistance, which ensures efficient Li<sup>+</sup> transport and stable interfacial contact. In addition, the overall porous structure and homogeneous particle dispersion remained well preserved, indicating that the amorphous carbon shell effectively accommodates the volume expansion and prevents particle agglomeration during repeated lithiation/delithiation processes. Moreover, *ex situ* XPS analysis was further employed to examine the surface chemistry of the Fe<sub>2</sub>O<sub>3</sub>@C-(8:2) electrodes before and after cycling (Fig. S4). Compared with the pristine electrode, the cycled sample showed the appearance of metallic Fe, while the main peaks of Fe 2p (~710–725 eV), O 1s (~530 eV), and C 1s (~285 eV) are still clearly observed which can be attributed to Fe<sub>2</sub>O<sub>3</sub> and carbon species. This indicates the reversible conversion between Fe<sup>3+</sup> and Fe<sup>0</sup> during the lithiation/delithiation process, consistent with the conversion mechanism described in eqn (4) and (5). Notably, after cycling, a new F 1s signal appeared, and the C 1s spectrum remained dominantly as C–C, C–O, C=O peaks, while the intensities of the C–O and π–π peaks slightly increased, suggesting the formation of a thin SEI layer composed of LiF, Li<sub>2</sub>CO<sub>3</sub>, and organic carbonate species. The absence of significant peak broadening indicates that the SEI is chemically stable and uniform, whereas the carbon shell retains its structural integrity, ensuring good electrical contact and effective mechanical buffering during repeated lithiation/delithiation cycles, which is consistent with the superior performance shown in Fig. 6a.

## 4 Conclusions

A novel core-shell-structured Fe<sub>2</sub>O<sub>3</sub>@C nanocomposite was synthesized using two facile steps, including sol-gel and pyrolysis processes, with bagasse-derived carbon as the carbon matrix. The effects of different Fe<sub>2</sub>O<sub>3</sub>-to-carbon ratios and polymeric binders (PVDF and PAA) on the electrochemical

performance of the anodes were systematically studied. Among the tested ratios, Fe<sub>2</sub>O<sub>3</sub>@C-(8:2) exhibited the best performance, delivering a high reversible capacity of 1893 mA h g<sup>-1</sup> after 100 cycles at 0.1 A g<sup>-1</sup> and 1553 mA h g<sup>-1</sup> after 350 cycles at 0.5 A g<sup>-1</sup>, along with excellent rate capability up to 3 A g<sup>-1</sup>. This enhancement was attributed to the optimized carbon coating, reduced charge-transfer resistance, and improved ionic/electronic conductivity. Furthermore, replacing PVDF with a PAA binder significantly improved the long-term stability owing to stronger mechanical adhesion and better interfacial contact. This study highlights the potential of low-cost, sustainable biomass-derived carbon combined with Fe<sub>2</sub>O<sub>3</sub> for the fabrication of efficient and stable anode materials for next-generation LIBs.

## Author contributions

Quoc Hai Nguyen: project administration, writing, review & editing, methodology. Chanwoo Park: methodology, formal analysis, writing. The Sang Chung: methodology, investigation. Thu Huyen Nguyen Thi: methodology, investigation. To Giang Tran: writing, formal analysis. Jong-Seong Bae: formal analysis. Tuan Loi Nguyen: writing – original draft, supervision. Jaehyun Hur: project administration, funding acquisition, review & editing.

## Conflicts of interest

There are no conflicts to declare.

## Data availability

All data supporting the findings of this study are available within the article and its supplementary information (SI). Supplementary information is available. See DOI: <https://doi.org/10.1039/d5ra07487h>.

## Acknowledgements

This research was supported by the Gachon University research fund of 2025 (GCU-202503380001) and Basic Science Research Capacity Enhancement Project through a Korea Basic Science Institute (National Research Facilities and Equipment Center) grant funded by the Ministry of Education (2019R1A6C1010016).

## References

- 1 Z. Meng, Z. Xu, H. Li, H. Xiong, X. Liu, C. Qin, *et al.*, Silicon/biomass carbon composite as a low-cost anode for lithium-ion batteries, *Energies*, 2025, **18**, 972.
- 2 P. Salimi, E. Venezia, S. Taghavi, S. Tieuli, L. Carbone, M. Prato, *et al.*, Lithium-Metal Free Sulfur Battery Based on Waste Biomass Anode and Nano-Sized Li<sub>2</sub>S Cathode, *Energy Environ. Mater.*, 2024, **7**, e12567.
- 3 K. Yan, Y. Zou, L.-X. Bao, Q. Xia, L.-Y. Meng, H.-C. Lin, *et al.*, Fluorinated N, P co-doped biomass carbon with high-rate



- performance as cathode material for lithium/fluorinated carbon battery, *Rare Met.*, 2025, **44**, 110–120.
- 4 L. Lin, S.-L. Tian, Z.-Y. Hu, Y. Zhang, L.-M. Chang, J.-J. Wang, *et al.*, Molecular crowding electrolytes for stabilizing Zn metal anode in rechargeable aqueous batteries, *Chin. Chem. Lett.*, 2024, **35**, 109802.
  - 5 S.-L. Tian, L. Lin, S.-Y. Jiang, L.-N. Song, H.-R. Wang, P. Nie, *et al.*, Ultra-long and rapid operating zinc metal batteries enabled by multifunctional polarizable interface stabilizer, *Chem. Eng. J.*, 2025, 167659.
  - 6 S.-Q. Li, K. Sun, Y.-Y. Liu, S.-L. Liu, J.-J. Zhou, W.-B. Zhang, *et al.*, Coupling Co<sub>2</sub>P nanoparticles onto N, P-doped biomass-derived carbon as efficient electrocatalysts for flexible Zn–air batteries, *Rare Met.*, 2024, **43**, 4982–4991.
  - 7 S.-L. Tian, L.-N. Song, L.-M. Chang, W.-Q. Liu, H.-F. Wang and J.-J. Xu, A magnetic/force coupling assisted lithium-oxygen battery based on magnetostriction and piezoelectric catalysis of CoFe<sub>2</sub>O<sub>4</sub>/BiFeO<sub>3</sub> cathode, *Nano Energy*, 2024, **126**, 109677.
  - 8 S. L. Tian, L. N. Song, L. M. Chang, W. Q. Liu, H. F. Wang and J. J. Xu, A Force-Assisted Li–O<sub>2</sub> Battery Based on Piezoelectric Catalysis and Band Bending of MoS<sub>2</sub>/Pd Cathode, *Adv. Energy Mater.*, 2024, **14**, 2303215.
  - 9 S.-L. Tian, M.-L. Li, L.-M. Chang, W.-Q. Liu and J.-J. Xu, A highly reversible force-assisted Li–CO<sub>2</sub> battery based on piezoelectric effect of BiO. 5NaO. 5TiO<sub>3</sub> nanorods, *J. Colloid Interface Sci.*, 2024, **656**, 146–154.
  - 10 N. Nitta, F. Wu, J. T. Lee and G. Yushin, Li-ion battery materials: present and future, *Mater. Today*, 2015, **18**, 252–264.
  - 11 M. Armand and J. M. Tarascon, Building better batteries, *Nature*, 2008, **451**, 652–657.
  - 12 S. Goriparti, E. Miele, F. De Angelis, E. Di Fabrizio, R. P. Zaccaria and C. Capiglia, Review on recent progress of nanostructured anode materials for Li-ion batteries, *J. Power Sources*, 2014, **257**, 421–443.
  - 13 H. B. Wu, J. S. Chen, H. H. Hng and X. W. Lou, Nanostructured metal oxide-based materials as advanced anodes for lithium-ion batteries, *Nanoscale*, 2012, **4**, 2526–2542.
  - 14 Y. Chen, X. Chen and Y. Zhang, A comprehensive review on metal-oxide nanocomposites for high-performance lithium-ion battery anodes, *Energy Fuels*, 2021, **35**, 6420–6442.
  - 15 Z. Li, Y. Mao, Q. Tian, W. Zhang and L. Yang, Extremely facile preparation of high-performance Fe<sub>2</sub>O<sub>3</sub> anode for lithium-ion batteries, *J. Alloys Compd.*, 2019, **784**, 125–133.
  - 16 H. Dong, M. Deng, D. Sun, Y. Zhao, H. Liu, M. Xie, *et al.*, Amorphous lithium-phosphate-encapsulated Fe<sub>2</sub>O<sub>3</sub> as a high-rate and long-life anode for lithium-ion batteries, *ACS Appl. Energy Mater.*, 2022, **5**, 3463–3470.
  - 17 Y. Huang, Z. Lin, M. Zheng, T. Wang, J. Yang, F. Yuan, *et al.*, Amorphous Fe<sub>2</sub>O<sub>3</sub> nanoshells coated on carbonized bacterial cellulose nanofibers as a flexible anode for high-performance lithium ion batteries, *J. Power Sources*, 2016, **307**, 649–656.
  - 18 Y.-M. Lin, P. R. Abel, A. Heller and C. B. Mullins,  $\alpha$ -Fe<sub>2</sub>O<sub>3</sub> nanorods as anode material for lithium ion batteries, *J. Phys. Chem. Lett.*, 2011, **2**, 2885–2891.
  - 19 X. Liu, W. Si, J. Zhang, X. Sun, J. Deng, S. Baunack, *et al.*, Free-standing Fe<sub>2</sub>O<sub>3</sub> nanomembranes enabling ultra-long cycling life and high rate capability for Li-ion batteries, *Sci. Rep.*, 2014, **4**, 7452.
  - 20 F. Qin, K. Zhang, L. Zhang, J. Li, H. Lu, Y. Lai, *et al.*, Sustainable synthetic route for  $\gamma$ -Fe<sub>2</sub>O<sub>3</sub>/C hybrid as anode material for lithium-ion batteries, *Dalton Trans.*, 2015, **44**, 2150–2156.
  - 21 A. D. Roberts, X. Li and H. Zhang, Porous carbon spheres and monoliths: morphology control, pore size tuning and their applications as Li-ion battery anode materials, *Chem. Soc. Rev.*, 2014, **43**, 4341–4356.
  - 22 J. Cheng, B. Wang, C. M. Park, Y. Wu, H. Huang and F. Nie, CNT@Fe<sub>3</sub>O<sub>4</sub>@C Coaxial Nanocables: One-Pot, Additive-Free Synthesis and Remarkable Lithium Storage Behavior, *Chem.–Eur. J.*, 2013, **19**, 9866–9874.
  - 23 F. Ahmed, G. Almutairi, P. M. Hasan, S. Rehman, S. Kumar, N. M. Shaalan, *et al.*, Fabrication of a biomass-derived activated carbon-based anode for high-performance li-ion batteries, *Micromachines*, 2023, **14**, 192.
  - 24 R. Liu, H. Liu, Q. Yang, Y. Ma, D. Dong and J. Wang, Longan-Derived Biomass Carbon-Induced Cubic-Type Ferric Oxide Nanoparticles for Efficient Lithium-Ion Battery Anodes, *Energy Fuels*, 2023, **37**, 16979–16987.
  - 25 M. A. Mahmud and F. R. Anannya, Sugarcane bagasse-A source of cellulosic fiber for diverse applications, *Heliyon*, 2021, **7**, e07771.
  - 26 S. Wu, Y. Jin, D. Wang, Z. Xu, L. Li, X. Zou, *et al.*, Fe<sub>2</sub>O<sub>3</sub>/carbon derived from peanut shell hybrid as an advanced anode for high performance lithium ion batteries, *J. Energy Storage*, 2023, **68**, 107731.
  - 27 J. Baruah, B. K. Nath, R. Sharma, S. Kumar, R. C. Deka, D. C. Baruah, *et al.*, Recent trends in the pretreatment of lignocellulosic biomass for value-added products, *Front. Energy Res.*, 2018, **6**, 141.
  - 28 F. Hajiali, T. Jin, G. Yang, M. Santos, E. Lam and A. Moores, Mechanochemical Transformations of Biomass into Functional Materials, *ChemSusChem*, 2022, **15**, e202102535.
  - 29 Q. H. Nguyen, I. T. Kim and J. Hur, Core-shell Si@c-PAN particles deposited on graphite as promising anode for lithium-ion batteries, *Electrochim. Acta*, 2019, **297**, 355–364.
  - 30 V. A. Agubra and J. W. Fergus, The formation and stability of the solid electrolyte interface on the graphite anode, *J. Power Sources*, 2014, **268**, 153–162.
  - 31 N. Paksung, J. Pfersich, P. J. Arauzo, D. Jung and A. Kruse, Structural Effects of Cellulose on Hydrolysis and Carbonization Behavior during Hydrothermal Treatment, *ACS Omega*, 2020, **5**, 12210–12223.
  - 32 H. Liang, K. Liu and Y. Ni, Synthesis of mesoporous  $\alpha$ -Fe<sub>2</sub>O<sub>3</sub> via sol–gel methods using cellulose nano-crystals (CNC) as template and its photo-catalytic properties, *Mater. Lett.*, 2015, **159**, 218–220.
  - 33 S. Álvarez-Torrellas, M. Munoz, J. Gläsel, Z. M. de Pedro, C. M. Domínguez, J. García, *et al.*, Highly efficient removal



- of pharmaceuticals from water by well-defined carbide-derived carbons, *Chem. Eng. J.*, 2018, **347**, 595–606.
- 34 M. Waqas, A. Aburizaiza, R. Miandad, M. Rehan, M. Barakat and A. Nizami, Development of biochar as fuel and catalyst in energy recovery technologies, *J. Clean. Prod.*, 2018, **188**, 477–488.
- 35 H. Wang, P. Hu, D. a. Pan, J. Tian, S. Zhang and A. A. Volinsky, Carbothermal reduction method for Fe<sub>3</sub>O<sub>4</sub> powder synthesis, *J. Alloys Compd.*, 2010, **502**, 338–340.
- 36 P. Liu, Y. Wang and J. Liu, Biomass-derived porous carbon materials for advanced lithium sulfur batteries, *J. Energy Chem.*, 2019, **34**, 171–185.
- 37 Q. H. Nguyen, S. So, Q. H. Nguyen, I. T. Kim and J. Hur, Mechanochemical synthesis of InP nanoparticles embedded in hybrid conductive matrix for high-performance lithium-ion batteries, *Chem. Eng. J.*, 2020, **399**, 125826.
- 38 G. Xia, N. Li, D. Li, R. Liu, C. Wang, Q. Li, *et al.*, Graphene/Fe<sub>2</sub>O<sub>3</sub>/SnO<sub>2</sub> ternary nanocomposites as a high-performance anode for lithium ion batteries, *ACS Appl. Mater. Interfaces*, 2013, **5**, 8607–8614.
- 39 C. Zhang, N. Qin, A. Pan, J. Yuan, Q. Liu, J. Ren, *et al.*, Hollow Fe<sub>2</sub>O<sub>3</sub> nanotubes derived from metal-organic framework for enhanced lithium storage and dye adsorption, *J. Porous Mater.*, 2021, **28**, 673–681.
- 40 Z. Li, Y. Mao, Q. Tian, W. Zhang and L. J. Yang, Extremely facile preparation of high-performance Fe<sub>2</sub>O<sub>3</sub> anode for lithium-ion batteries, *J. Alloys Compd.*, 2019, **784**, 125–133.
- 41 Y. Wang, J. Han, X. Gu, S. Dimitrijević, Y. Hou and S. Zhang, Ultrathin Fe<sub>2</sub>O<sub>3</sub> nanoflakes using smart chemical stripping for high performance lithium storage, *J. Mater. Chem. A*, 2017, **5**, 18737–18743.
- 42 Y.-M. Lin, P. R. Abel, A. Heller and C. B. Mullins,  $\alpha$ -Fe<sub>2</sub>O<sub>3</sub> nanorods as anode material for lithium ion batteries, *J. Phys. Chem. Lett.*, 2011, **2**, 2885–2891.
- 43 J. Li, L. Christensen, M. N. Obrovac, K. C. Hewitt and J. R. Dahn, Effect of heat treatment on Si electrodes using polyvinylidene fluoride binder, *J. Electrochem. Soc.*, 2008, **155**, A234–A238.
- 44 S. J. An, J. Li, C. Daniel, D. Mohanty, S. Nagpure and D. L. Wood III, The state of understanding of the lithium-ion-battery graphite solid electrolyte interphase (SEI) and its relationship to formation cycling, *Carbon*, 2016, **105**, 52–76.
- 45 J. G. Xu, Q. L. Zhang and Y. T. Cheng, High capacity silicon electrodes with nafion as binders for lithium-ion batteries, *J. Electrochem. Soc.*, 2016, **163**, A401–A405.
- 46 N. Nitta, D. N. Lei, H. R. Jung, D. Gordon, E. B. Zhao, G. Gresham, *et al.*, Influence of binders, carbons, and solvents on the stability of phosphorus anodes for li-ion batteries, *ACS Appl. Mater. Interfaces*, 2016, **8**, 25991–26001.
- 47 A. D. Roberts, X. Li and H. J. Zhang, Porous carbon spheres and monoliths: morphology control, pore size tuning and their applications as Li-ion battery anode materials, *Chem. Soc. Rev.*, 2014, **43**, 4341–4356.
- 48 J. Cheng, B. Wang, C. M. Park, Y. Wu, H. Huang and F. J. Nie, CNT@ Fe<sub>3</sub>O<sub>4</sub>@ C Coaxial Nanocables: One-Pot, Additive-Free Synthesis and Remarkable Lithium Storage Behavior, *Chem.–Eur. J.*, 2013, **19**, 9866–9874.
- 49 Q. H. Nguyen, H. Kim, I. T. Kim, W. Choi and J. Hur, Few-layer NbSe<sub>2</sub>@ graphene heterostructures as anodes in lithium-ion half-and full-cell batteries, *Chem. Eng. J.*, 2020, **382**, 122981.
- 50 N. Y. Kim, I. Kim, B. Bornemann, V. Presser, H. Ueda, H. J. Lee, *et al.*, Recent Advances in Nanoengineering of Electrode-Electrolyte Interfaces to Realize High-Performance Li-Ion Batteries, *Energy Environ. Mater.*, 2024, **7**, e12622.

